International Journal of Solids and Structures 251 (2022) 111737

Contents lists available at ScienceDirect

International Journal of Solids and Structures

journal homepage: www.elsevier.com/locate/ijsolstr

Peeling mechanics of film-substrate system with mutually embedded nanostructures in the interface

Langquan Shui [a,1], Weidong Yan [a,1], Yujie Zhang [a], Lihan Xu [a], Enlai Gao [a], Ze Liu [a,b,*], Quanshui Zheng [c,*]

[a] Department of Engineering Mechanics, School of Civil Engineering, Wuhan University, Wuhan, Hubei 430072, PR China
[b] State Key Laboratory of Water Resources & Hydropower Engineering Science, Wuhan University, Wuhan 430072, PR China
[c] Department of Engineering Mechanics, Tsinghua University, Beijing 100084, PR China

ARTICLE INFO

Keywords:
Peeling
Adhesion
Structured interface
Nanomolding/nanoimprinting
Mechanical demoulding

ABSTRACT

Through mechanical deformation of crystalline metals with hard molds, superplastic nanomolding provides a simple and high-throughput method to directly form nanostructures in the metal surface. The releasing of the molded nanostructures generally involves in chemical etching away the mold, in which metal nanostructures could also be chemically attacked. Therefore, mechanical demoulding is very promising not only for solving the above problem, but also for drastically reducing the cost by recycling molds. As a result, the mechanics underlying the mechanical demoulding is very important and highly desired since it can tell what kind of nanofeatures can be released without damaging the molds. In this paper, we develop a theory for the peeling mechanics of elastic film with its surface nanostructures deeply embedded in a substrate. Specifically, by analyzing the obtained micromechanical behavior in the interface and combining it into the mechanical framework of the macro-bending behavior of the film, we successfully derive a nonlinear governing equation for demoulding. By non-dimensionalizing the governing equation and further numerically solving it, we find out a simple expression for the apparent adhesion work. Our theory demonstrates that the apparent adhesion work is mainly contributed by the interface shear stress rather than the interface energy as revealed by the peeling of elastic film from flat or wavy interfaces, and the fillet radius at the edge of the cavity is found to be a crucial factor to determine the success or failure of demoulding. Finally, by recording the real-time peeling force of an actual peeling process, we observe that the theoretical prediction is in good agreement with the experimental results. This work not only provides theoretical guidance for mechanical demoulding of molded micro-/nanostructures, but also establishes a mechanical framework for studying the peeling mechanics of real material interface.

1. Introduction

Film peeling is a classical mechanical problem, the earliest research can be traced back to the study on adhesion and peeling of mica by Obreimoff (1930). After that, the basic mechanical model of film peeling (the well-known Kendall peeling model) was established (Kendall, 1971, 1975; Rivlin, 1944). In the follow-up study, further consideration of inertia effect (Kinloch and Williams, 2002), dependence of peeling rate (Barthel, 2008; Creton and Ciccotti, 2016; Dalbe et al., 2014; Gent and Petrich, 1969; Muller, 1999; Persson and Brener, 2005; Shui et al., 2020; Shull, 2002; Tiwari et al., 2017; Villey et al., 2015), evolution of interfacial structure (Ghatak et al., 2004; Kaelble, 1971, 1992; Yu et al., 2017), bio-adhesion (Khandeparker and Anil, 2007; Kong et al., 2008; Yin et al., 2005) and hysteresis (Israelachvili, 1992) are continuously enriching the breadth and depth of the research on peeling mechanics. Recently, the rapid development of superplastic nanomolding of metals to directly form large-area nanofeatures in metal surface and the highly desired mechanical demoulding of molded nanostructures require to extend the peeling mechanics to a film-substrate system with mutually embedded nanostructures in the interface (Liu et al., 2022).

Nanomolding refers to a top-down fabrication method where a moldable material is shaped using a hard mold (Chou et al., 1997;

* Corresponding authors at: Department of Engineering Mechanics, School of Civil Engineering, Wuhan University, Wuhan, Hubei 430072, PR China (Ze Liu).
E-mail addresses: ze.liu@whu.edu.cn (Z. Liu), zhengqs@tsinghua.edu.cn (Q. Zheng).
[1] These authors contribute equally.

https://doi.org/10.1016/j.ijsolstr.2022.111737
Received 19 June 2021; Received in revised form 23 April 2022; Accepted 22 May 2022
Available online 24 May 2022

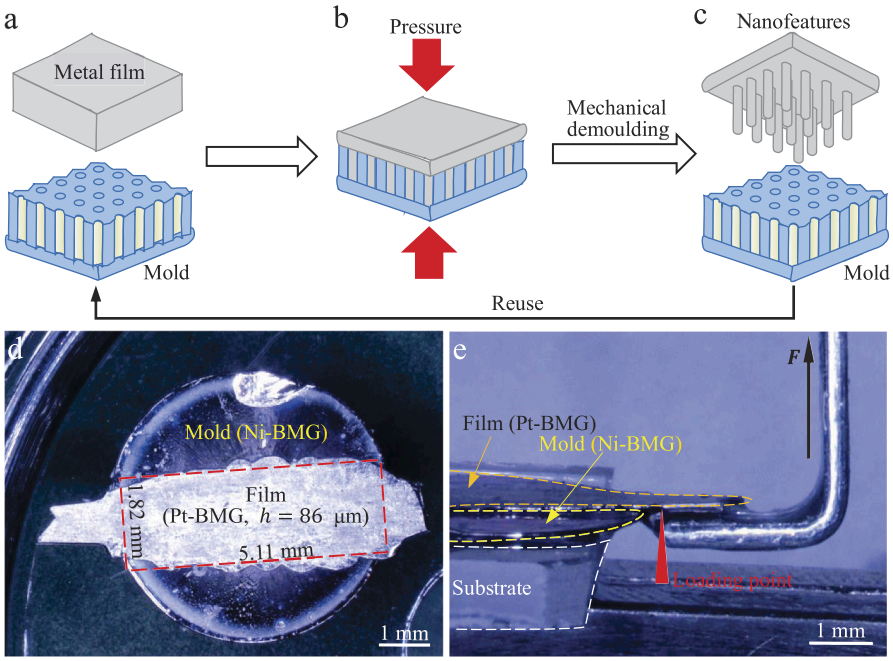

Fig. 1. (a)-(c) Illustrations of superplastic nanomolding of metals by using reusable hard mold. (d) A Pt-BMG film was pressed into a Ni-BMG ($Ni_{60}Pd_{20}P_{17}B_3$) mold with nanocavities arrays. The Ni-BMG mold was fabricated by compressing a Ni-BMG disc against a Si mold (with nanorods in the surface, the diameter of the nanorods is 500 nm) at 390°C, the mean loading pressure and time were 137 MPa (3.35 kN at 24.4 mm^2) and 150 s, respectively. The replicated Ni-BMG nanocavities arrays were subsequently freed from the Si mold by immersing the sample in KOH solution (with concentration of 6 mol/L, 70°C) for 5 hours, and then cleaned with deionized water and ethanol. (e) Typical experimental set-up for mechanical demoulding of formed Pt-BMG film in (d).

Kumar et al., 2009; Liu, 2017). Before 2017, nanomolding has been mainly achieved in amorphous materials such as polymers (Chou et al., 1996; Guo, 2004; Xia and Whitesides, 1998) and bulk metallic glasses (Kumar et al., 2009; Li et al., 2016). The associated mechanism has been documented originating from viscous flow (Chiu et al., 2009; Graham, 2006; Liu and Schroers, 2015), superimposed with capillary effect (Golden et al., 2013). Until recently, superplastic nanomolding in the crystalline state has been introduced for a very broad range of metals and alloys (Liu et al., 2020; Liu, 2017, 2019; Liu et al., 2019). It was found that the atomic diffusion itself can be the dominant deformation mechanism on the nanoscale (Liu et al., 2020; Liu et al., 2019).

Although nanomolding provides a high-throughput way to prepare nanofeatures in variety of materials, most applications require free standing nanorods. Therefore, dissolution of molds through chemical etching is generally used, which increases the cost of mold consumption. Especially, many materials immersion in acidic or alkaline solutions will lead to the partial or even complete dissolution of the formed nanostructures. Alternatively, mechanical demoulding has thus been explored (Singer et al., 2015; Xu et al., 2020), where the thinner part (can be either the moldable material or mold) is directly peeled from the formed combinations (refer to Section 2). Therefore, the mold can be recycled and the fabrication cost can be drastically reduced (Xu et al., 2020). Moreover, based on this strategy, free standing nanorods of any moldable materials can be directly obtained because the process is free from chemical etching. However, it is observed that only when the length of molded nanorods is short, can the nanorods be mechanically demoulded without damage (Xu et al., 2020). Otherwise, the nanorods will break and leave in the mold surface (refer to Section 2). To provide theoretical guidance for the mechanical demoulding, the mechanics of peeling structured elastic film from embedded substrate should be considered.

Though peeling of adhered flat (Kendall, 1971, 1975; Rivlin, 1944) and waved (Guduru and Bull, 2007; Peng and Chen, 2015) films has been well investigated, the corresponding mechanics for mechanical demoulding of embedded micro/nanostructures are less well developed (Li et al., 2018). In this study, combining theoretical modeling with peeling measurement, the interface shear and pull-out resistance of each nanopillar are proven to be the two main contributions to the apparent adhesion work of peeling an interface with embedded nanostructures. This is different from the generally studied peeling of flat or wavy interface where the apparent adhesion work mainly comes from the interface adhesion energy. Besides, the apparent adhesion work is found inversely proportional to the interfacial debonding length in the early stage of peeling, and is approximately linear with the length of the embedded nanopillars. Moreover, the fillet at the entrance of the mold cavities is distinguished as a crucial determinant of the success of mechanical demoulding.

The rest of the paper is organized as follows. In Section 2, experiments of nanomolding and mechanical demoulding, and corresponding model description are presented. By studying the deformation and stress states of embedded pillars (Section 3.1), and then deriving the apparent adhesion work of the structured interface (Section 3.2), the peeling behavior is theoretically analyzed in Section 3. Finally, brief concluding remarks are given in Section 4.

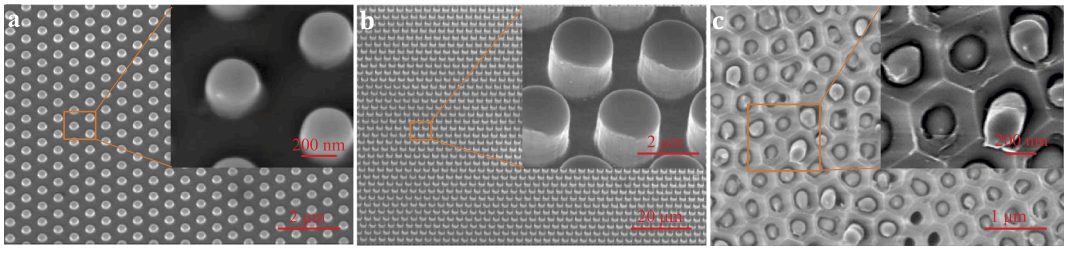

Fig. 2. (a)-(b) Prepared Al nanorods/microrods arrays by superplastic nanomolding of bulk Al and following mechanical demoulding (Xu et al., 2020). (c) Break of InBiSn nanorods arrays in the AAO mold during mechanical demoulding.

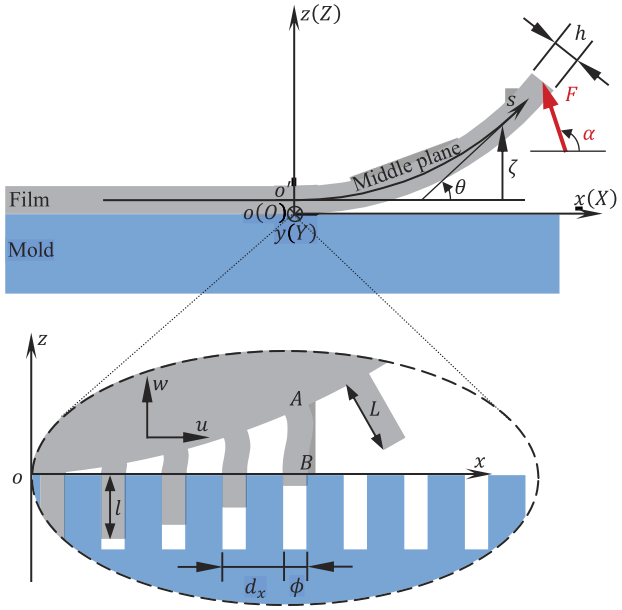

Fig. 3. Peeling model of an elastic film with its surface pillars embedded in a substrate.

2. Experiments and model description

2.1. Experimental set-up and observations

The experimental process is briefly shown in Fig. 1(a)-(c), where a metal film is pressed into a mold. To increase the molding efficient, high temperature is generally needed. The formed combinations are then mechanically demoulded by directly peeling the thinner part. Typical result is shown in Fig. 1(d), where a Pt-BMG ($Pt_{57.3}Cu_{14.6}Ni_{5.3}P_{22.8}$) strip sheet which cut from a prepressed Pt-BMG disc (forming from zero to 4 kN at 260°C, the loading rate was 0.5 mm/min) was compressed against a prepared Ni-BMG nanomolds at 260°C with a loading force of 3 kN (The preparation of the Ni-BMG nanomolds refers to the descreptions in Fig. 1). Finally, the formed Pt-BMG sheet was peeled along the direction perpendicular to the sheet by sticking one end of the Pt-BMG strip sheet to a clamp (Fig.1(e)) using quick adhesive, the clamp was fixed onto a force sensor (MTI SEM Tester-100). The peeling process was monitored under an optical microscopy (KEYENCE VHX-5000) and the peeling force (F) during the mechanical demoulding process was recorded by the controlling software of the MTI SEM Tester-100. Typical results of prepared metal nanorods by using the abovementioned method are shown in Fig. 2. When the length of molded nanorods is short, the molded nanorods are mechanically demoulded without damage (Fig. 2(a) and (b)). However, for longer nanorods, it is observed that the nanorods break and leave in the mold surface (Fig. 2(c)).

2.2. Model description

Note that both the size and spacing of the nanorods are several orders of magnitude smaller than the film thickness in experiments (Fig. 1(d) and Fig. 2), as a result, the "lattice" distribution of nanorods (Fig. 2) has little effect on the overall deflection of the film, and deflection of the film can be approximated as two dimensional. Considering the typical mechanical demoulding process (Fig. 3), the peeling force can be generally along any direction. For simplicity, we assume the mold as a rigid substrate because the deformation mainly occurs in the microrods/nanorods and the thin film during mechanical demoulding. The current and material coordinates are described in the same coordinate system ($oxyz$ or $OXYZ$) (Fig. 3). The origin o is located at the interfacial crack tip. The y–axis is perpendicular to the paper and points inward. The thickness (along z-axis) and width (along y–axis) of the film are h and b, respectively. The deflection, curvature and rotation of the middle plane (along the natural coordinate $o's$) are denoted by ζ, κ and θ, respectively. The displacement of the material point (X, Y, Z) in the film is

$$\boldsymbol{u}(X, Y, Z) = (u, v, w) = (x - X, y - Y, z - Z),$$

where (x, y, z) represent the current coordinates of the material point, v is zero under the plane strain assumption, and $w = \zeta$ at the middle plane. In the surface of the mold, there are arrays of cavities with a diameter of ϕ, the periods along x and y–axis are d_x and d_y, respectively. Accordingly, in the surface of the film, there are molded pillars arrays with the same diameter and period as the mold cavities. The initial total length and embedded depth of a pillar (along z-axis) are L and l, respectively.

The Young's modulus and Poisson's ratio of the film are E and ν, respectively. The apparent adhesion work of the micro-structured interface is denoted as $\Delta\gamma$. The intrinsic adhesion work between the film and the mold is $\Delta\gamma_0$. The surface energy of the film and the mold is denoted by γ_F and γ_M, respectively, and the corresponding interface energy between them is denoted by γ_{FM}. By ignoring the effects of air, we have

$$\Delta\gamma_0 = \gamma_F + \gamma_M - \gamma_{FM}. \tag{1}$$

When the free end of the film is far from the origin, the Kendall's peeling model (Kendall, 1971, 1975; Menga et al., 2018) gives the relationship between the peeling force (F) and the apparent adhesion work ($\overline{\Delta\gamma}$) as

$$\overline{\Delta\gamma} = \frac{F}{b}\left(1 - \cos\alpha + \frac{\varepsilon_F}{2}\right), \tag{2a}$$

where α is the peeling angle (Fig. 3), and $\varepsilon_F = F/(Ehb)$ is the tensile strain near the free end of the film. It is noted that α can be larger than π, which can be experimentally realized by rolling the peeled part onto a small roller (as schematically shown in Fig. 10 (b)). Considering that the deformation of film cannot exceed its elastic limit in order to avoid damage during mechanical demoulding, then we have $\varepsilon_F < 2\%$ for metallic glasses and $\varepsilon_F < 0.2\%$ for typical metals. Experimentally, such strain constraint can be satisfied by preparing a sufficiently thick film and setting the peeling angle far away from 0 and 2π (i.e., $0 \ll \alpha \ll 2\pi$). For example, given $\alpha = \pi/2$, $\overline{\Delta\gamma}$=50 N/m, E=94.8 GPa (Pt-BMG; Wang (2012)), Eq. (2a) yields a film thickness requirement as $h > 26$ nm. Under these experimental conditions, one notes that $1 - \cos\alpha \gg \varepsilon_F/2$, i.e., the film extension along s–axis can be ignored if the completely peeled part of the film is sufficiently long (e.g., the situation in Section 3.2.1). Then Eq. (2a) can be simplified as

$$\overline{\Delta\gamma} = \frac{F}{b}(1 - \cos\alpha), 0 \ll \alpha \ll 2\pi. \tag{2b}$$

Note that the total deformation of the film in Fig. 3 can be divided into two parts, i.e., the local deformation near the action location of the constraint of the substrate, and the global bending deformation of the film. The global displacement of the film surface at Z=0 can be directly given as

$$\begin{cases} u_0 = u|_{Z=0} = X - \displaystyle\int_0^X \cos\theta \mathrm{d}X + \frac{h}{2}\sin\theta, \\ w_0 = w|_{Z=0} = \zeta + \dfrac{h}{2}(1 - \cos\theta), \end{cases} \tag{3}$$

where θ is related with s, X, κ and ζ as

$$\frac{\mathrm{d}X}{\mathrm{d}s} = \cos\theta, \frac{\mathrm{d}\zeta}{\mathrm{d}s} = \sin\theta, \kappa = \frac{\mathrm{d}\theta}{\mathrm{d}s}.$$

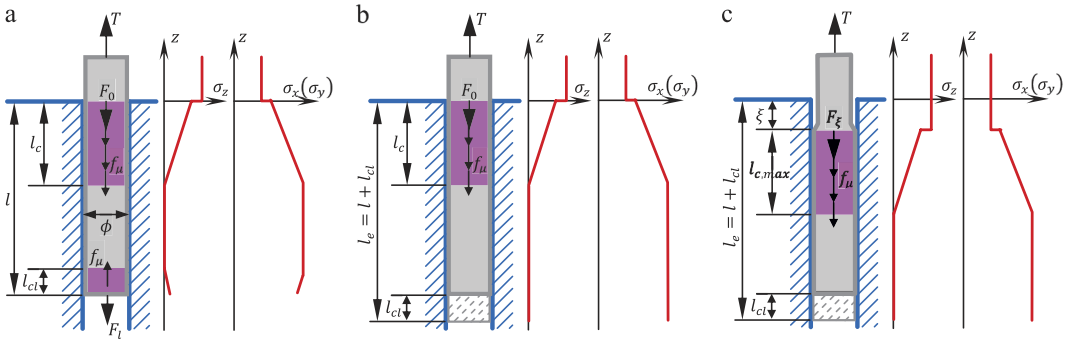

Fig. 4. Stress evolution during pulling out an embedded pillar. (a)-(b) The situations without interface separation. (c) The situation with interface separation. l is the embedded depth. l_c and l_{cl} represent the length of the pillar that is in contact with the cavity (violet region), and stressed in balance with loads T and F_l, respectively.

3. Theoretical analysis of the peeling behavior

3.1. Mechanical behavior of the pillars

3.1.1. Tangential reaction force (along z-axis) from the cavity

A simplified pull-out model of a pillar is considered as shown in Fig. 4 (a), where a pillar is embedded in a semi-infinite stiff cavity with an embedded depth of l. A pulling-out force T is applied to the upper cross-section of the pillar. Under the pulling-out force, the shear reaction force at the contact interface between the pillar and the cavity can be assumed to be proportional to the contact area. Thus, the shear force (along z–axis) per unit length is (Fig. 4(a))

$$f_\mu = -\pi\phi\mu. \tag{4}$$

where μ is the interface shear strength. Considering that the cavity is stiff, the effect of radial pressure (pressure on the side of a pillar) can be ignored. Assuming that the pillar is slender, the primary beam theory can be adopted, and the shear force exerted on the pillar is equivalent to the tensile force along the axis of the pillar for simplification.

Considering that the interface energy is important at the micro/nano-scale. During the pulling-out process, the initially contacted line between the pillar and the cavity (near the cavity edge) may separate (interface separation cannot occur at the lower end of the pillar), then the upper contact line moves downward (with a movement distance of ξ, Fig. 4(c)). The surface/interface energy thus induces tension along z–axis at $z = -\xi$ and $z = -l$. Physically, at $z = -\xi = 0$, the pulling-out process increases the free surface of the pillar, and thus induces tension as (the interface between the cavity and the pillar keeps closed throughout, Fig. 4(a) and (b))

$$F_0 = -\pi\phi\gamma_F. \tag{5}$$

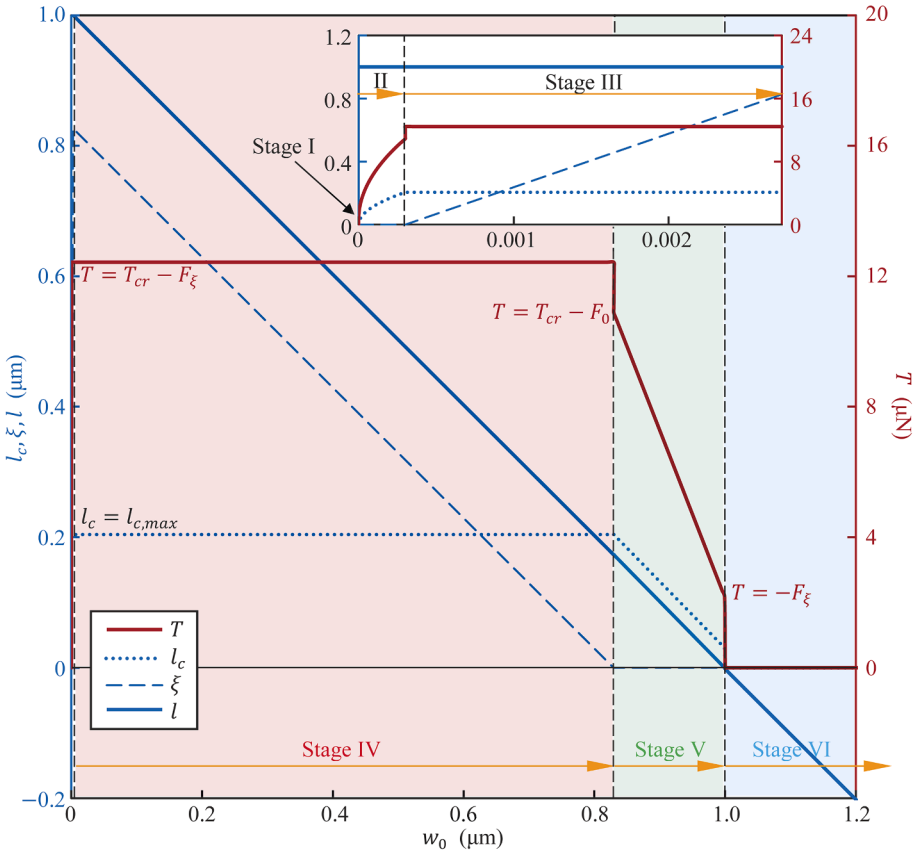

Fig. 5. Quasi-static pulling-out process of a pillar with respect to w_0. The expressions for the calculations refer to Table 1. Typical values of material and geometric parameters are used: $\phi = 0.2$ μm, $L = 1$ μm, $\varepsilon_0 = -0.00175$ (i.e., $\sigma_0 = -186$ MPa); $E = 69$ GPa, $\nu = 0.35$; $\mu = 80$ MPa; $\gamma_F = 1$ N/m, $\gamma_M = 3$ N/m, $\gamma_{FM} = 0.5359$ N/m.

Table 1
Key parameters of the pulling-out process of an embedded pillar ($\Sigma = \nu(2\gamma_F + \phi\sigma_0)$)

Stage	T	l_c	ξ	l	w_0
I	0 to $-F_0$	0	0	L	0
II	$-F_0$ to $T_{cr} - F_\xi$	$\begin{cases} (T+F_0)/(\pi\mu\phi), T < T_{cr} - F_0 \\ T_{cr}/(\pi\mu\phi), T \geq T_{cr} - F_0 \end{cases}$	0	L	$\frac{\nu}{1-\nu}\frac{2\mu}{\lambda\phi}l_c^2$
III	$T_{cr} - F_\xi$	$T_{cr}/(\pi\mu\phi)$	0 to $l_e - l_c$	L	$\frac{\nu}{1-\nu}\frac{2\mu}{\lambda\phi}l_c^2 + \frac{2\xi}{E\phi}(2\mu l_c + \Sigma) - \frac{\nu}{1-\nu}\frac{2\mu}{\lambda\phi} \bullet \begin{cases} 0, \xi \leq L - l_c \\ (\xi + l_c - L)^2, \xi > L - l_c \end{cases}$
IV	$T_{cr} - F_\xi$	$T_{cr}/(\pi\mu\phi)$	$l_e - l_c$ to 0	$\xi + l_c - l_{cl}$	$\frac{\nu}{1-\nu}\frac{2\mu}{\lambda\phi}\left(l_c^2 - l_{cl}^2\right) + \frac{1}{E\phi}(4\mu l_c + 2\Sigma + E\phi)(L - l_c + l_{cl}) - \xi$
V	$T_{cr} - F_\xi$ to $-F_\xi$	$\begin{cases} T_{cr}/(\pi\mu\phi), T \geq T_{cr} - F_0 \\ (T+F_0)/(\pi\mu\phi), T < T_{cr} - F_0 \end{cases}$	0	$l_c - l_{cl}$	$\frac{\nu}{1-\nu}\frac{2\mu}{\lambda\phi}\left(l_c^2 - l_{cl}^2\right) + \frac{1}{E\phi}\left(\frac{4T}{\pi\phi} + 2\Sigma + E\phi\right)(L - l)$
VI	$-F_\xi$ to 0	0	0	0 to $-\infty$	$2L\Sigma/(E\phi) + L - l$

At $z = -\xi < 0$, the pulling-out process increases the free surface of both the pillar and the cavity and induces tension as (Fig. 4(c))

$$F_\xi = -\pi\phi\Delta\gamma_0. \tag{6}$$

At $z = -l$, the pulling-out process increases the free surface of the cavity and induces tension as (Fig. 4(a))

$$F_l = -\pi\phi(\gamma_M - \gamma_{FM}). \tag{7}$$

The deformation induced by F_l is inherent and can be included in the reference configuration when considering the deformation induced by T. F_l causes an upward shear force at the interface, which will be overcome when the two violet regions (pink regions in Fig. 4(a)) are in contact. To facilitate the calculation of the pulling-out force (without regard to the change of local stress state of the pillar near its free surface), one can virtually extend the embedded length from l to (Fig. 4(b) and (c))

$$l_e = l + l_{cl}, \tag{8}$$

where l_{cl} is the maximum action length (along z–axis) caused by F_l (Fig. 4(a)) and can be derived as

$$l_{cl} = \frac{\gamma_M - \gamma_{FM}}{\mu}. \tag{9}$$

Generally, the pulling-out process of a long enough pillar (the pulling-out a short pillar can be degenerated from the pulling-out of a long pillar (refer to Fig. 5)) can be divided into six stages. At stage I, $\xi = 0$, the pulling-out force increases until F_0 is reached. At this stage, the global elastic deformation can be ignored. At stage II , $\xi = 0$, as the pulling-out force increases, the elastic deformation region (l_c in Fig. 4(a) and (b)) of the embedded part gradually extends downward, and the shear reaction force also increases. Once the interface is separated, the elastic deformation region reaches the maximum ($l_c = l_{c,max}$, Fig. 4(c)). At stage III (Fig. 4(c)), $\xi > 0$, l_c keeps constant ($l_c \equiv l_{c,max}$), and the deformation at the range of $Z > \xi$ will be uniform. At this stage, the pulling-out force is also a constant. As the pulling-out displacement increases, the violet region in Fig. 4(c) moves downward as a whole, until it touches the bottom of the pillar and further overcomes F_l. At stage IV, as the pulling-out displacement increases, the whole pillar slides upward, and ξ gradually decreases to 0. But the pulling-out force remains constant as before. At stage V, $\xi = 0$, as the pulling-out displacement increases, both the pulling-out force and the violet region gradually decrease. Finally, l_e decreases to l_{cl}, and the pillar is completely separated from the mold.

The whole pulling-out process is further described in Table 1, where the derivation of the expressions is based on the stress states. w_0 is the pulling-out displacement which can be calculated by $w_0 = w|_{Z=0}$ (Eq. (3)). T_{cr} represents the critical pulling-out force that can keep the interface open (without considering F_ξ). By letting $\sigma_x = -2\gamma_F/\phi$ and $T = T_{cr}$ at $z = -\xi < 0$, one can obtain T_{cr} as

$$T_{cr} = \frac{1-\nu}{4\nu}\left(2F_0 - \pi\phi^2\sigma_0\right). \tag{10}$$

During the quasi-static pulling-out process (without considering gravity), T cannot be larger than T_{cr}, i.e., the maximum pull-out force is independent of the pillar length if it is long enough. Initially (i.e., $l = L$ and $0 \leq T \leq T_0$), all stress components in the pillar should be zero except the stresses of

$$\sigma_x = \sigma_y = \sigma_0 = \frac{E\varepsilon_0}{1-\nu},$$

where σ_0 and ε_0 are the radial mismatch stress and strain, respectively. The mismatch can be from the plastic forming induced residual deformation or temperature change induced thermal mismatch. The mismatch strain is assumed uniform along the pillar. One can derive the normal stress in the pillar as (Fig. 4(b) and (c))

$$\sigma_x = \sigma_y = \begin{cases} -\frac{2\gamma_F}{\phi}, z > -\xi, \\ \sigma_0 + \frac{\nu}{1-\nu}\sigma_z, -l_e \leq z \leq -\xi, \end{cases} \tag{11a}$$

and

$$\sigma_z = \begin{cases} \frac{4T}{\pi\phi^2}, z > -\xi, \\ \frac{4\mu}{\phi}(l_c + z + \xi), -l_c - \xi \leq z \leq -\xi, \\ 0, -l_e \leq z \leq -l_c - \xi, \end{cases} \tag{11b}$$

where l_c is given in Table 1. According to the Hooke's law and the geometric equations, Eq. (11) yields the displacement along z–axis of the pillar as

$$w = \begin{cases} \frac{\nu}{1-\nu}\frac{2\mu}{\lambda\phi}l_c^2 + \frac{2}{E\phi}\left(\frac{2T}{\pi\phi} + 2\nu\gamma_F + \nu\phi\sigma_0\right)(z+\xi) + L - l - \delta, z \geq -\xi, \\ \frac{\nu}{1-\nu}\frac{2\mu}{\lambda\phi}(z + \xi + l_c)^2 + L - l - \delta, -l_c - \xi \leq z \leq -\xi, \\ L - l - \delta, -l_e \leq z \leq -l_c - \xi, \end{cases} \tag{12}$$

where $\lambda = E\nu/(1+\nu)/(1-2\nu)$ is the Lame constant, and

$$\delta = \begin{cases} \frac{\nu}{1-\nu}\frac{2\mu}{\lambda\phi}(\xi + l_c - l)^2, l < l_c + \xi, \\ 0, l \geq l_c + \xi. \end{cases}$$

Based on the expressions in Table 1, the pull-out process can be quantified as shown in Fig. 5. It is clear that the pulling-out displacement in the first three stages is very small and can be ignored. Thus, only the stages IV and V need to be considered in the following discussions, and we have

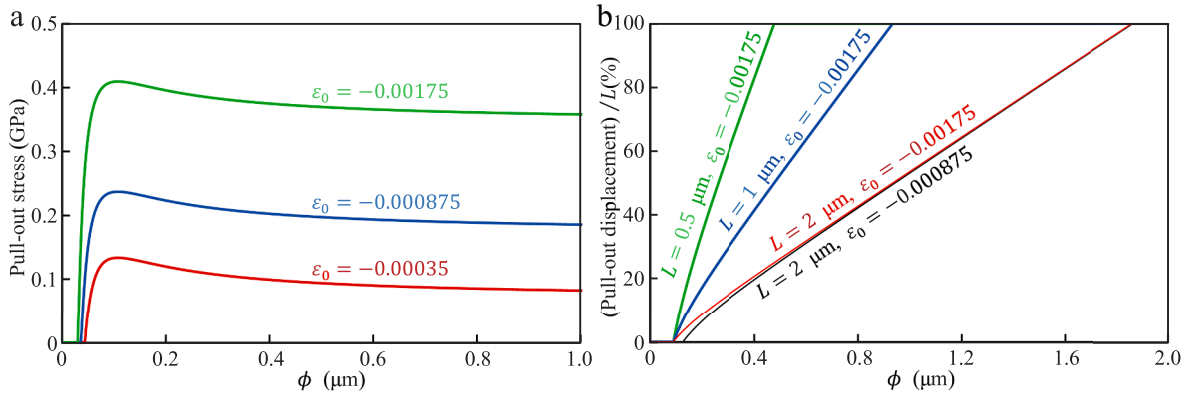

Fig. 6. Effect of ϕ on the pull-out process: (a) The pull-out stress at stage IV can be calculated by $4(T_{cr}+\pi\phi\Delta\gamma_0)/(\pi\phi^2)$ (Eq. (14a)) , which is independent of L. (b) The proportion of the pulling-out displacement at stage V (with respect to the total pull-out length) equals to $(F_l+T_{cr})/(\pi\mu\phi L)$ if $0 < (F_l+T_{cr})/(\pi\mu\phi) < L$, equals to 0 if $(F_l+T_{cr})/(\pi\mu\phi) \le 0$, and equals to 100% if $(F_l+T_{cr})/(\pi\mu\phi) \ge L$). The material parameters refer to Fig. 5.

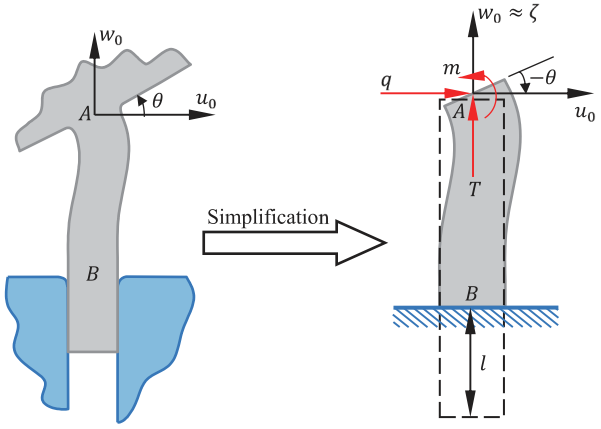

Fig. 7. Deformation of a partially pulled-out pillar.

$$w_0 \approx L - l, \tag{13}$$

and

$$T \approx \begin{cases} T_{cr} + \pi\phi\Delta\gamma_0, 0 \le w_0 \le L - \dfrac{F_l + T_{cr}}{\pi\mu\phi}, \\ \pi\phi(\mu L + \Delta\gamma_0 - \mu w_0), L - \dfrac{F_l + T_{cr}}{\pi\mu\phi} < w_0 \le L, \\ 0, w_0 > L. \end{cases} \tag{14a}$$

where $0 \le w_0 \le L-(F_l+T_{cr})/(\pi\mu\phi)$ refers to the stage IV, where the pulling-out force is a constant $(T_{cr} + \pi\phi\Delta\gamma_0)$; $L-(F_l+T_{cr})/(\pi\mu\phi) < w_0 \le L$ refers to the stage V, where the pulling-out force decreases linearly. Based on Eq. (14a), the effect of ϕ on the pull-out process can be calculated (Fig. 6). If $\phi \le -2\gamma_F/\sigma_0 + 4\nu/(1-\nu) \bullet \Delta\gamma_0/\sigma_0$, the pillar tends to separate from the cavity automatically. In reality, this may not occur because the separation involves in local deformation of the film; if $\phi \gg -2\gamma_F/\sigma_0 + 4\nu/(1-\nu) \bullet \Delta\gamma_0/\sigma_0$, T at stage IV tends to be a constant and is determined by σ_0 (or ε_0), and when $\phi \to -2\gamma_F/\sigma_0 + 4\nu/(1-\nu) \bullet \Delta\gamma_0/\sigma_0$ from the right side, T appr oaches to zero rapidly after a slight increase. If $\phi \ge -2\gamma_F/\sigma_0 - 4\nu/(1-\nu) \bullet (\mu L + \gamma_M - \gamma_{FM})/\sigma_0$, only stage V exists; and if $\phi \le -2\gamma_F/\sigma_0 - 4\nu/(1-\nu) \bullet (\gamma_M - \gamma_{FM})/\sigma_0$, only stage IV exists. In addition, there is an approximate linear relationship between the pulling-out displacement and ϕ at stage V, and the radial mismatch stress (strain) has a slight effect when ϕ is a relatively large.

In the above discussion, L is considered large enough. If L is small (pull-out short pillars), the pull-out process changes. Based on Fig. 5, one can directly move the four continuous curves of the stage IV-VI to the left by a distance ΔL to obtain the pull-out behavior of a pillar with length of $L-\Delta L$. In this operation, each continuous curve of stages IV-VI has one intersection with the corresponding curve of stages I-III, which divides a continuous curve into two parts (if the intersection is at the end, the intersection itself is one part). By deleting the left part of a continuous curve of stages IV-VI and the right part of the corresponding curve of stages I-III, and then combining the rest two curves into one continuous curve, one obtains the pull-out behavior of a pillar with length of $L-\Delta L$. Note that stage IV will completely disappear when $L \to (F_l+T_{cr})/\pi\mu\phi$ (refer to Eq. (14a)).

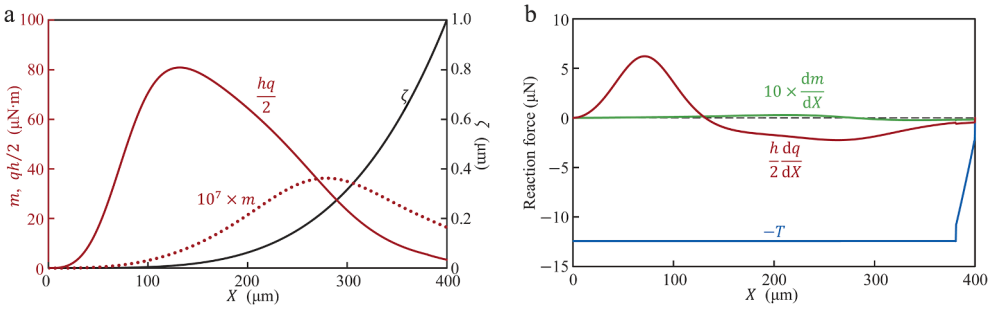

Fig. 8. Reactions exerted on partially pulled-out pillars located at different distances (X) (Fig. 9). (a) Dependence of m, q, ζ on X. (b) Calculated reaction forces (i.e., $-T$, $-\mathrm{d}(q\zeta)/\mathrm{d}X$ and $\mathrm{d}m/\mathrm{d}X$; refer to Eq. (27)). Typical values of $d_x = d_y = 0.3$ μm, $h = 10$ μm and $\epsilon = 4$ nm were used in the calculations. Other material and geometric parameters refer to Fig. 5. ζ is assumed as $\epsilon + 7.716 \times 10^{22} X^4$.

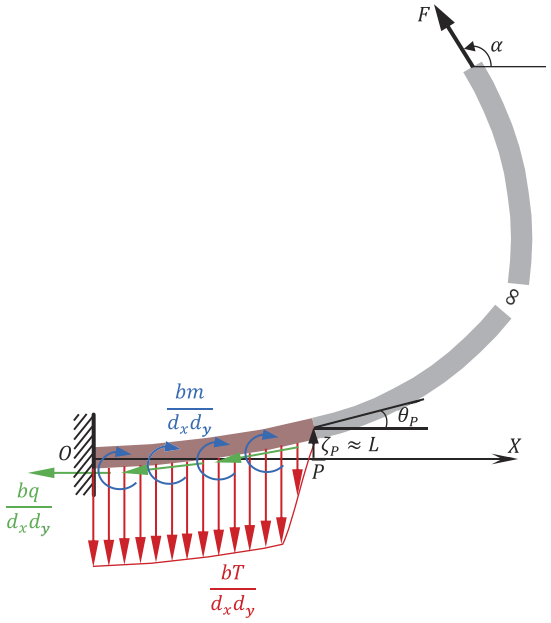

Fig. 9. Sketch the deformation of a film under actions of a far-field tension (F) and homogenized interface forces (m, q and T) from partially pulled-out pillars (refer to Section 3.2.2).

When considering the effect of stress exerted on the elastic film from the partially pulled-out pillars (Fig. 3 and Fig. 9), as a conservative estimate, one can consider T as a constant, i.e.,

$$T \approx \begin{cases} T_{cr} + \pi\phi\Delta\gamma_0, w_0 \le L > \dfrac{F_l + T_{cr}}{\pi\mu\phi}, \\ \pi\phi(\mu L + \Delta\gamma_0), w_0 \le L \le \dfrac{F_l + T_{cr}}{\pi\mu\phi}, \\ 0, w_0 > L. \end{cases} \tag{14b}$$

3.1.2. Deformation of the partially pulled-out pillars

For the partially pulled-out pillar as shown in left of Fig. 7, local deformation of the film (point A in Fig. 3), the axial deformation of the pillar, and effect of the lateral displacement (u_0) on the vertical displacement at $Z = 0$ are ignored. The displacement u_0 can be assumed far less than w_0. Thus, the model in the left of Fig. 7 can be simplified to the one in the right of Fig. 7. The pillar at point A suffers forces from the film (moment m, horizontal force q, and vertical force T). Our finite element analysis indicates that the shear deformation cannot be ignored. The governing equation for deformation of the partially pulled-out pillar can be given as

$$\frac{E\pi\phi^4}{64}\frac{\partial^4 u}{\partial Z^4} - T\frac{\partial^2 u}{\partial Z^2} = 0, Z \in [-w_0, 0], \tag{15}$$

with boundary conditions of

$$\begin{cases} u|_{Z=0} = u_0, \\ \left.\dfrac{\partial u}{\partial Z}\right|_{Z=0} = -\theta + \gamma, \\ u|_{Z=-w_0} = 0, \\ \left.\dfrac{\partial u}{\partial Z}\right|_{Z=-w_0} = \gamma, \end{cases}$$

where $\gamma = \chi q$ is the shear induced rotation. u_0 and w_0 refer to Eq. (3). For a Timoshenko beam with circular cross-section, the constant χ is determined as

$$\chi = \frac{7 + 6\nu}{3E\pi\phi^2/4}$$

The general solution of Eq. (15) is

$$u = C_1 + C_2 Z + C_3\cosh(kZ) + C_4\sinh(kZ), \tag{16}$$

where

$$C_1 = \frac{ku_0w_0 - \theta/k + \theta w_0/(2K) - K(u_0 + \gamma w_0 - \theta w_0/2)}{kw_0 - 2K},$$

$$C_2 = \frac{ku_0 + K(\theta - 2\gamma)}{kw_0 - 2K},$$

$$C_3 = \frac{\theta/k - \theta w_0/(2K) - K(u_0 - \gamma w_0 + \theta w_0/2)}{kw_0 - 2K},$$

$$C_4 = \frac{(\gamma - \theta)w_0 - u_0 + \theta K/k}{kw_0 - 2K},$$

$$K = \tanh\frac{kw_0}{2}, k = \frac{8}{\phi^2}\sqrt{\frac{T}{E\pi}}.$$

On the other hand, according to the moment balance,

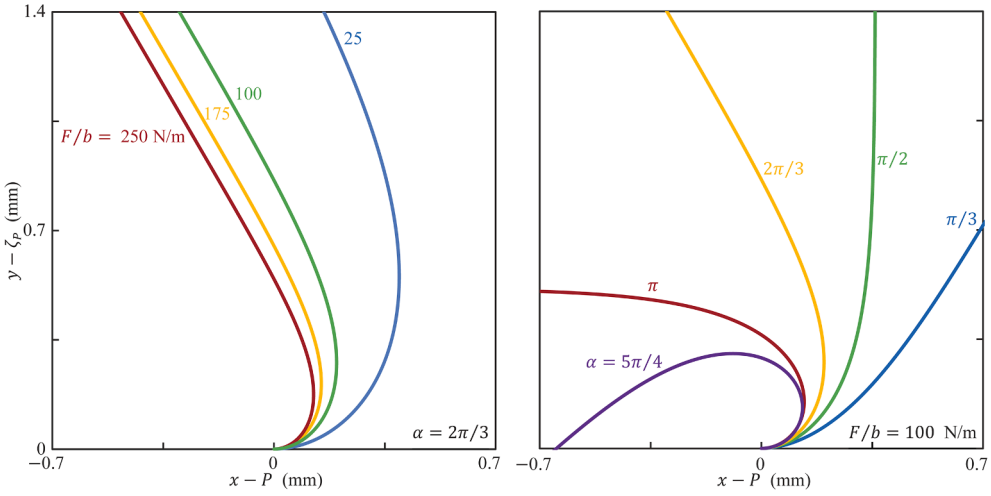

Fig. 10. Configuration of the completely peeled part ($x \ge P$) in Fig. 9, where θ_P is set as 0.01. Left: the situations with a constant $\alpha = 2\pi/3$ and different F/b. Right: the situations with a constant $F/b = 100$ and different α. The material and geometric parameters refer to Fig. 8.

$$\frac{E\pi\phi^4}{64}\frac{\partial}{\partial Z}\left(\frac{\partial u}{\partial Z}-\gamma\right) = -m-qZ-T(u_0-u), \tag{17}$$

which yields

$$u = u_0+\frac{m}{T}+\frac{q}{T}Z+C_3\cosh(kZ)+C_4\sinh(kZ). \tag{18}$$

Based on Eqs. (16) and (18), one has

$$m = \frac{qw_0-Tu_0}{2}+\frac{T\theta}{2kK}, \tag{19}$$

and

$$q = \frac{(\theta K+ku_0)T}{2K(\chi T-1)+kw_0}. \tag{20a}$$

Positive directions of m and q follow the arrows in Fig. 7. It can be verified that the effect of q is always far more significant than that of m as shown in Fig. 8. Under the condition of small deflection, Eq. (20a) can be approximated as

$$q \approx \frac{h}{2\chi\zeta}\frac{\mathrm{d}\zeta}{\mathrm{d}X}. \tag{20b}$$

As indicated by Eqs. (19) and (20), the reaction forces and moment exerted on partially pulled out pillars can be fully described by u_0, w_0, θ and T.

In addition, it is noteworthy that m and q will become infinite when $w_0\to 0$, which is due to the failure of the beam model. In reality, the cavity is elastic and the edge of the cavity is filleted (with a radius of $\epsilon \ll \phi$), therefore, the real fixed end is at $Z=\epsilon$. In other words, w_0 in Eqs. (19) and (20) should be replaced by $w_0+\epsilon$ when calculating m and q. Figure 8 shows the calculated m and q on a partially pulled-out pillar caused by the bending deformation of the film, where we considered a simple deflection as $\zeta\propto X^4$.

3.2. The apparent adhesion work of the micro-structured interface

Generally, at the initial peeling stage, the peeling force approaches to zero, and then rapidly increases. As the peeling process progresses, the peeling force will gradually decrease to a stable value. At the stable peeling process, considering that $L\ll h$, the deflection of the film in the partially peeled part ($X\le P$, $X=P$ is solution of the equation $w_0(X)=L$, Fig. 9) is small. While the deflection of the film in the completely peeled part ($X\ge P$) can be very large if assuming the initial length of such part is infinite. In this section, the deformation of these two parts will be discussed separately.

3.2.1. Deformation of the completely peeled part ($X\ge P$) of the film

Considering that the deformation of the thin film is concentrated near $X=P$, the film can be assumed to have infinite length (Fig. 9). The deflection and rotation of the film at $X=P$ are denoted as $\zeta_P\approx L$ and θ_P, respectively. Bending of such film (with large deflection) should satisfy

$$\frac{\mathrm{d}^2\theta}{\mathrm{d}s^2} = \frac{F}{Db}\sin(\theta-\alpha) \tag{21}$$

where $D=Eh^3/[12(1-\nu^2)]$ is the bending stiffness. The boundary conditions are

$$\begin{cases}\theta|_{s=P}=\theta_P,\\ \theta|_{s=+\infty}=\alpha.\end{cases}$$

The solution of Eq. (21) reads

$$s = P-\sqrt{\frac{Db}{F}}\ln\left(\tan\frac{\alpha-\theta}{4}\cot\frac{\alpha-\theta_P}{4}\right), \tag{22a}$$

or parametrically as

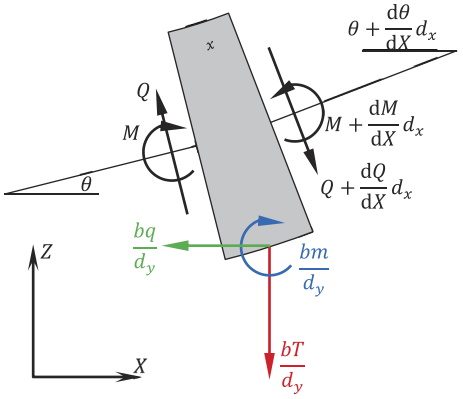

Fig. 11. Forces on an infinitesimal section element of the film with sizes $d_x\times b\times h$. Considering $\theta\to 0$, the force balance along Z–axis yields $d_x\mathrm{d}Q/\mathrm{d}X=-bT/d_y$, and the moment balance yields $d_x\mathrm{d}M/\mathrm{d}X=Qd_x+b(m+qh/2)/d_y$, where Q and M are the sectional shear force and moment, respectively. Note that the effect of the sectional tension in the film can be ignored considering that in our experiments, the film thickness is usually 2-3 orders of magnitude larger than the diameter or the length of the pillars, and the peeling angle is usually around $\pi/2$.

$$\begin{cases} x = P+(s-P)\cos\alpha-2\sqrt{\frac{Db}{F}}\left(\cos\frac{\alpha+\theta}{2}-\cos\frac{\alpha+\theta_P}{2}\right),\\ y = \zeta_P+(s-P)\sin\alpha-2\sqrt{\frac{Db}{F}}\left(\sin\frac{\alpha+\theta}{2}-\sin\frac{\alpha+\theta_P}{2}\right).\end{cases} \tag{22b}$$

Based on Eq. (22), the deformation of the completely peeled part ($X\ge P$) of the film can be predicted precisely (Fig. 10), and the moment at $x\approx X=P$ (i.e., $s=P$) can be calculated as

$$M_P = Db\frac{\mathrm{d}\theta}{\mathrm{d}s}\Big|_{\theta=\theta_P} = 2\sqrt{DbF}\sin\frac{\alpha-\theta_P}{2}. \tag{23}$$

Combing Eq. (23) with Eq. (2b) and given $\alpha\gg\theta_P$, it is found that

$$\overline{\Delta\gamma} = \frac{M_P^2}{2Db^2}. \tag{24}$$

The sectional shear force at $x\approx X=P$ is

$$Q_P = F\sin(\theta_P-\alpha),$$

and one can derive a relation as

$$\tan\frac{\alpha-\theta_P}{2} = -\frac{M_P^2}{2DbQ_P}. \tag{25}$$

It will be shown that Eqs. (24) and (25) are useful for the analysis of the adhesion work (referring to Section 3.2.2).

3.2.2. Deformation of the partially peeled part ($X\le P$) of the film

The deflection of the partially peeled part is small compared to the size of the film (Fig. 9), but it may not be ignored by comparison with the size of the pillars. Thus, Eq. (3) can be approximated as

$$\begin{cases} u_0\approx\frac{1}{2}h\theta,\\ w_0\approx\zeta,\end{cases} \tag{26}$$

where the high order terms of θ are ignored, and

$$\theta\approx\frac{\mathrm{d}\zeta}{\mathrm{d}X}.$$

Then the bending curvature can be expressed as

$$\kappa = \frac{d\theta}{ds} \approx \frac{d\theta}{dX} \approx \frac{d^2\zeta}{dX^2}.$$

Considering that $d_x \ll h$, the discrete loads exerted on the film by the pillars can be approximately considered continuous along x-axis. Then the force and moment balance of the infinitesimal section element in Fig. 11 gives

$$d_x\frac{dQ}{dX} + \frac{bT}{d_y} = 0,\ d_x\frac{dM}{dX} = Qd_x + \left(m + \frac{qh}{2}\right)\frac{b}{d_y},$$

where Q is the sectional shear force, M is the sectional moment. By substituting

$$M = Db\kappa$$

into the above equation, one obtains

$$d_x d_y D\frac{d^4\zeta}{dX^4} - \frac{d}{dX}\left(m + \frac{qh}{2}\right) + T = 0, X \in [0, P]. \tag{27}$$

Note that the interface adhesion (in XOY plane) can induces complex deformation near $X = 0$. For simplification, the contribution from the interface adhesion (in XOY plane) is equivalently added to T, i.e., T is updated by $T + d_x d_y \rho_F \Delta\gamma_0 / L$, where $\rho_F = 1 - \rho_M$ and

$$\rho_M = \frac{\pi\phi^2/4}{d_x d_y}$$

is the area fraction of the mold cavities. Considering that the deflection of the partially peeled part ($X \le P$) is always very small, the effect of m can be ignored (Section 3.1.2), Eq. (27) can then be simplified as (by using Eq. (20b))

$$d_x d_y D\frac{d^4\zeta}{dX^4} - \frac{h^2}{4\chi}\frac{d}{dX}\frac{d\zeta}{\zeta dX} + T + d_x d_y\frac{\rho_F\Delta\gamma_0}{L} = 0, X \in [0, P]. \tag{28}$$

The sectional shear force Q and the total moment Ξ corresponding to Eq. (28) read

$$Q = \frac{d\Xi}{dX}, \Xi = Db\frac{d^2\zeta}{dX^2} - \frac{bh^2}{4d_x d_y \chi}\ln\frac{\zeta}{\epsilon};$$

and the boundary conditions of Eq. (28) are

$$\begin{cases} \zeta|_{X=0} = \epsilon, \\ \left.\dfrac{d\zeta}{dX}\right|_{X=0} = 0, \\ \Xi|_{X=0} = 0, \\ \zeta|_{X=P} = L + \epsilon, \\ \Xi|_{X=P} = M_P, \\ Q|_{X=P} = Q_P. \end{cases}$$

By introducing dimensionless parameters of (Eq. (14b) is adopted)

$$\widehat{\zeta} = \frac{(7+6\nu)(t+t_0)}{9\rho_M h(1-\nu^2)}\zeta, \widehat{X} = \frac{\sqrt{t+t_0}}{h}X; \widehat{P} = \frac{\sqrt{t+t_0}}{h}P;$$

$$t = \frac{16(7+6\nu)}{3E\pi\phi^2}T = \begin{cases} \dfrac{16(7+6\nu)}{3E\phi}\left(\Delta\gamma_0 - \dfrac{1-\nu}{2\nu}\gamma_F\right) - \dfrac{4(7+6\nu)\varepsilon_0}{3\nu}, L > \dfrac{F_l + T_{cr}}{\pi\mu\phi}, \\ \dfrac{16(7+6\nu)}{3E\phi}(\Delta\gamma_0 + \mu L), L \le \dfrac{F_l + T_{cr}}{\pi\mu\phi}; \end{cases}$$

$$t_0 = \frac{\rho_F}{\rho_M}\frac{4(7+6\nu)}{3EL}\Delta\gamma_0;$$

Eq. (28) becomes

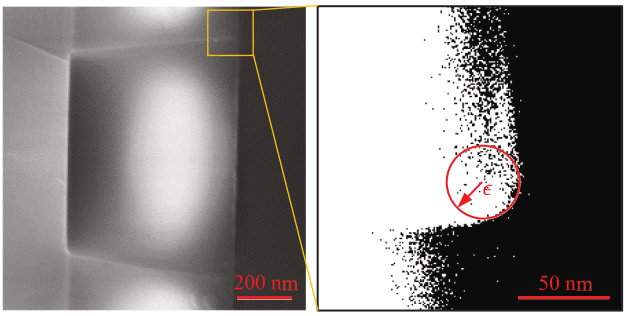

Fig. 12. The fillet radius (ϵ) at the edge of a mold cavity used in our experiments (measured based on the SEM image in OXZ plane). Several samples were measured to generate an average value of ϵ.

$$\frac{d^4\widehat{\zeta}}{d\widehat{X}^4} - \frac{d}{d\widehat{X}}\frac{d\widehat{\zeta}}{\widehat{\zeta}d\widehat{X}} + 1 = 0, \widehat{X} \in [0, \widehat{P}]. \tag{29a}$$

Correspondingly, the dimensionless sectional shear force and the total moment can be derived as

$$\widehat{Q} = \frac{d^3\widehat{\zeta}}{d\widehat{X}^3} - \frac{d\widehat{\zeta}}{\widehat{\zeta}d\widehat{X}}, \widehat{\Xi} = \frac{d^2\widehat{\zeta}}{d\widehat{X}^2} - \ln\frac{\widehat{\zeta}}{\widehat{\epsilon}}; \widehat{\epsilon} = \frac{(7+6\nu)(t+t_0)}{9\rho_M(1-\nu^2)}\frac{\epsilon}{h}.$$

Further, Eq. (29a) can be rewritten as

$$\widehat{Q} = \widehat{Q}_0 - \widehat{X}, \widehat{X} \in [0, \widehat{P}], \tag{29b}$$

or

$$\widehat{\Xi} = \widehat{\Xi}_0 + \widehat{Q}_0\widehat{X} - \frac{1}{2}\widehat{X}^2, \widehat{X} \in [0, \widehat{P}], \tag{29c}$$

where $\widehat{Q}_0 = \widehat{Q}|_{\widehat{X}=0}$, $\widehat{\Xi}_0 = \widehat{\Xi}|_{\widehat{X}=0}$. Finally, one can express the dimensionless boundary conditions as (under the condition of $\alpha \gg \theta_P$)

$$\begin{cases} \widehat{\zeta}|_{\widehat{X}=0} = \widehat{\epsilon}, \\ \left.\dfrac{d\widehat{\zeta}}{d\widehat{X}}\right|_{\widehat{X}=0} = 0, \\ \left.\dfrac{d^2\widehat{\zeta}}{d\widehat{X}^2}\right|_{\widehat{X}=0} = 0, \\ \widehat{\zeta}|_{\widehat{X}=\widehat{P}} = \widehat{L} = \dfrac{(7+6\nu)(t+t_0)}{9\rho_M(1-\nu^2)}\dfrac{L+\epsilon}{h}, \\ \widehat{M}_P = \widehat{\Xi}|_{\widehat{X}=\widehat{P}} = \dfrac{4(7+6\nu)}{3E\rho_M bh^2}M_P, \\ \widehat{Q}_P = \widehat{Q}|_{\widehat{X}=\widehat{P}} = \dfrac{4(7+6\nu)}{3E\rho_M bh\sqrt{t+t_0}}Q_P. \end{cases}$$

Though $\widehat{\Xi}$ and $\widehat{Q}$ can be easily solved analytically based on Eqs. (29b) and (29c), the deflection $\widehat{\zeta}$ is difficult to be solved analytically. The shooting method was adopted to solve $\widehat{\zeta}$. Because of the singularity when $\widehat{\zeta} \to 0$, the numerical solution are usually difficult to converge unless all the boundary conditions are set with proper values at the location of $\widehat{\zeta} \to 0$ (i.e., $\widehat{X} = 0$). Specifically, we first set the boundary conditions at $\widehat{X} = 0$, i.e. $\widehat{\zeta}|_{\widehat{X}=0} = \widehat{\epsilon}$, $d\widehat{\zeta}/d\widehat{X}|_{\widehat{X}=0} = d^2\widehat{\zeta}/d\widehat{X}^2|_{\widehat{X}=0} = 0$, and try different $\widehat{Q}_0$ values. Then the solutions are used to match a group of $\widehat{L}$, $\widehat{M}_P$, and $\widehat{Q}_P$. By establishing the mapping relations among $\widehat{Q}_0$, $\widehat{L}$, $\widehat{M}_P$, and $\widehat{Q}_P$, one can finally obtain the solutions of Eq. (29).

Considering a group of typical parameters as $\epsilon = 20$ nm (it is measured as ~17 nm in our experiment, Fig. 12), $h = 0.15$ mm, $\rho_M = 0.35$, $\widehat{L} = 0.0004$, $\nu = 1/3$, $t + t_0 \sim 0.036$, and $\widehat{Q}_0 = 0.05625$, the solution of Eq. (29) is obtained and displayed in Fig. 13(a). It is found

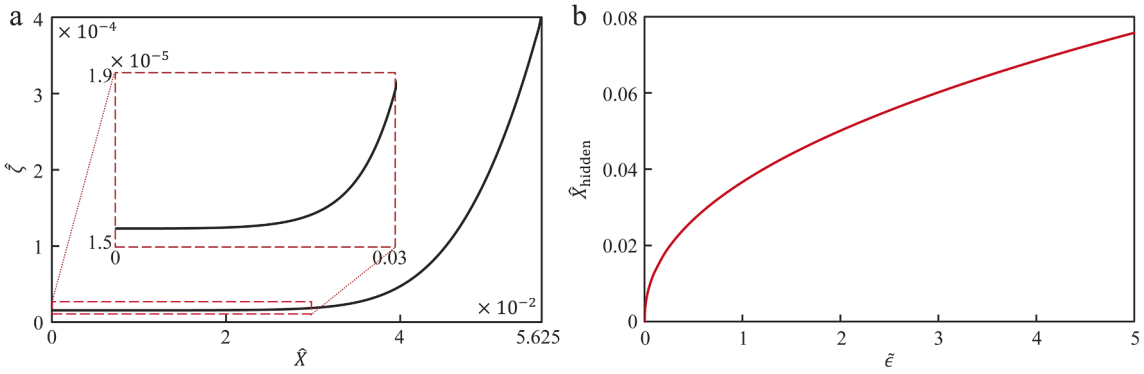

Fig. 13. (a) A deflection curve of the film based on numerical solution of Eq. (29) ($\widetilde{\epsilon}$=1 is used in the calculation). (b) Effects of $\widetilde{\epsilon}$ on the hidden length of the interfacial crack ($\widehat{X}_{\text{hidden}}$).

that most of the partially peeled part of the film has little deflection due to the interfacial shear constraint (in *OXY* plane), which is quite different from the common behavior of cantilever beam. The predictions indicate that the interfacial shear will result in the real crack tip (at $\widehat{X} \sim 0$) far from the visual location (i.e., $\widehat{X} \sim 0.03 \sim 0.6\widehat{P}$ in Fig. 13 (a)), in other words, a large part of the interfacial crack seems to be "hidden". The location of the hidden length of the interfacial crack can be determined as $\widehat{X}_{\text{hidden}}$ at $\widehat{\zeta} = 2\widehat{\epsilon}$ (note that the deflection $\widehat{\zeta} \geq \widehat{\epsilon}$), that is, $\widehat{X}_{\text{hidden}}$ is determined by $\widehat{\epsilon}$, which is shown in Fig. 13(b), where $\widetilde{\epsilon} = \widehat{\epsilon}/\widehat{\epsilon}_{\text{ref}}$, $\widehat{\epsilon}_{\text{ref}} = 1.543 \times 10^{-5}$. The results show that smaller fillet can effectively reduce the hidden length of the interfacial crack, this is because the smaller the fillet, the stronger the shear constraint in *OXY* plane (when $\widetilde{\epsilon} \to 0$, $q|_{\widehat{X}\sim 0} \to \infty$, Eq. (20)), so the influence depth (along $-x$–axis) of the peeling force decreases.

3.2.3. The apparent adhesion work and interfacial shear stress (in OXY plane)

By using the dimensionless parameters, Eqs. (24) and (25) become

$$\overline{\Delta\gamma} = \frac{27(1-\nu^2)}{8(7+6\nu)^2} Eh\rho_M^2 \widehat{\Delta\gamma}, \tag{30}$$

and

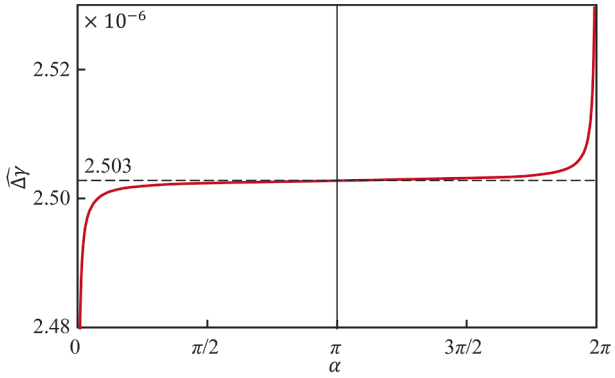

Fig. 14. Theoretically predicted relationship between the dimensionless apparent adhesion work $\widehat{\Delta\gamma}$ (Eq. (30)) and the peeling angle α (Eq. (31)).

In fact, when $\alpha = \pi$, $\widehat{Q}_P = 0$, i.e., the section at $\widehat{X} = \widehat{P}$ only bears a bending moment. Eq. (33) can significantly simplify the numerical solving process. In addition, it is noted that $\widehat{\Delta\gamma}$ is only determined by $\widehat{\epsilon}$ and $\widehat{L}$, the relation between $\widehat{\Delta\gamma}$ and $\widehat{L}$ can thus be readily obtained (Fig. 15(a)). It is observed that when $\widehat{L} \gg \widehat{\epsilon}$, $\widehat{\Delta\gamma}$ is approximately proportional to $\widehat{L}$

$$\widehat{\Delta\gamma} \approx \left(0.159\widetilde{\epsilon}^3 + 2.070\widetilde{\epsilon} + 0.968\right) \times 10^{-3}\widehat{L} - \frac{0.369\widetilde{\epsilon}^3 - 2.085\widetilde{\epsilon}^2 - 1.884\widetilde{\epsilon} + 1.743}{\widetilde{\epsilon} + 0.310} \times 10^{-6} \tag{34}$$

$$\tan\frac{\alpha}{2} = -\frac{9\rho_M(1-\nu^2)\widehat{M}_P^2}{2(7+6\nu)\sqrt{t+t_0}\widehat{Q}_P}, \tag{31}$$

where

$$\widehat{\Delta\gamma} = \widehat{M}_P^2 \tag{32}$$

is the dimensionless apparent adhesion work.

Given the parameters in Fig. 13(a), and considering $\widehat{Q}_0 \in [0.0561, 0.0564]$, one can solve Eq. (29) and calculate $\widehat{\Delta\gamma}$ based on Eqs. (30) and (31), as demonstrated in Fig. 14. It is found that $\widehat{\Delta\gamma}$ is related to the peeling angle α. However, when α is far from 0 or 2π, $\widehat{\Delta\gamma}$ can be approximated as a constant

$$\widehat{\Delta\gamma} \approx \widehat{\Delta\gamma}|_{\alpha=\pi}, 0 \ll \alpha \ll 2\pi. \tag{33}$$

By substituting Eq. (34) into Eq. (30), the apparent adhesion work $\overline{\Delta\gamma}$ can be calculated. Eq. (34) indicates that $\widehat{\Delta\gamma}$ will remain unchanged if one keeps $(7+6\nu)/(1-\nu^2) \bullet (t+t_0)/(h\rho_M)$ as a constant. The effects of ρ_M, h, L, and ϕ on $\overline{\Delta\gamma}$ can be roughly summarized as

$$\overline{\Delta\gamma} \propto \begin{cases} \dfrac{\rho_M hL}{\phi}, L > \dfrac{F_l + T_{cr}}{\pi\mu\phi}, \\ \dfrac{\rho_M hL^2}{\phi}, L \leq \dfrac{F_l + T_{cr}}{\pi\mu\phi}. \end{cases} \tag{35}$$

On the other hand, based on the numerical solutions, one can evaluate the interfacial strength (in *OXY* plane). The analysis in Section 3.1.2 (Fig. 8(a)) reveals that the shear failure of a pillar at its root (point A in Fig. 3) would be the major failure mode during peeling. According

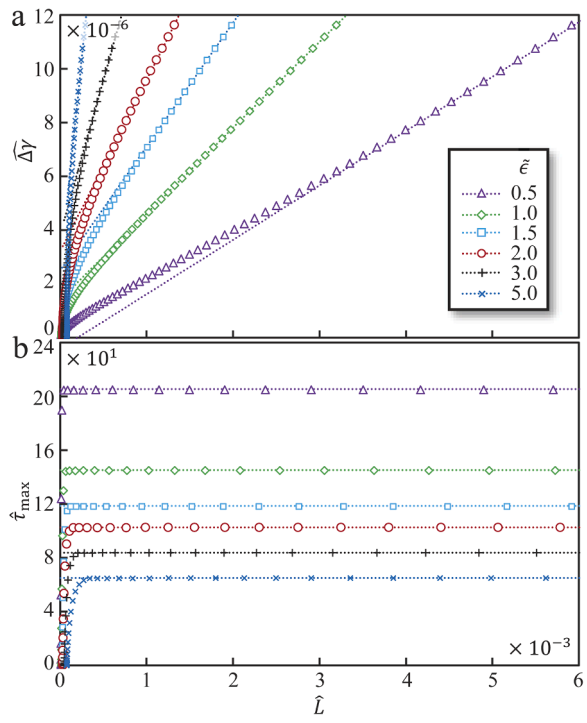

Fig. 15. Theoretically predicted dimensionless apparent adhesion work $\widehat{\Delta\gamma}$ (a) and the maximum interfacial shear stress $\hat{\tau}_{max}$ (b) versus the pillar length, where $\tilde{\epsilon} = \hat{\epsilon}/\hat{\epsilon}_{ref}$. The data points are obtained by numerical solutions, the dotted lines are drawn based on Eqs. (34) and (36).

to the expression of q (Eq. (20b)), one can introduce a dimensionless shear stress as $\hat{\tau} = d\hat{\zeta}/(\hat{\zeta}d\hat{X})$. When $\hat{L} \gg \hat{\epsilon}$, the numerical solutions yields a fitted relation among $\hat{\tau}$, $\hat{\epsilon}$ and $\hat{L}$ as

$$\hat{\tau}_{max} = \max_{0 \le X \le P}\{\hat{\tau}\} \approx \frac{145}{\sqrt{\hat{\epsilon}}} \approx \frac{1}{\sqrt{3.07\hat{\epsilon}}}, \tag{36}$$

which indicates that the shear stress only depends on $\hat{\epsilon}$ when $\hat{L} \gg \hat{\epsilon}$ (Fig. 15(b)).

Based on Eqs. (34)-(36), a map of $\widehat{\Delta\gamma}$ and $\hat{\tau}_{max}$ (with respect to $\hat{\epsilon}$ and $\hat{L}$) can be obtained (Fig. 16). For a given shear strength, the permitted parameter space is limited above the corresponding contour line. For example, for a given shear strength of $4q_{max}/(\pi\phi^2) = 2\hat{\tau}_{max}\sqrt{t+t_0}/(\pi\phi^2\chi) = 100$ MPa and $\nu = 1/3$, $t + t_0 = 10^{-8}$, and $E = 70$ GPa, one have $\hat{\tau}_{max} = 85.71$, which yields $\hat{\epsilon} = 4.434 \times 10^{-5}$ or $\tilde{\epsilon} = 2.874$. Meanwhile, to ensure safe peeling, the parameters should be taken from the region above the line of $\hat{\epsilon} = 4.434 \times 10^{-5}$ (the dashed line in Fig. 16). Fig. 16 tells the larger $\hat{\epsilon}$ the weaker the interfacial shear stress and the less the structural failure. On the other hand, a smaller $\hat{\epsilon}$ is more conducive to peeling/demoulding, which seems contradictory because $q|_{\hat{X}\sim 0} \to \infty$ when $\tilde{\epsilon} \to 0$ (Eq. (20)). In fact, such behavior can be predicted by Fig. 13(b), which shows that a smaller $\tilde{\epsilon}$ leads to a smaller $\hat{X}_{hidden}$, and thus a smaller peeling force (with constant tension $t + t_0$ and the same $\hat{L}$).

3.2.4. *Near-field peeling behavior*

The above peeling model can be called a standard peeling model since an infinite long (along X–axis) film is considered. The peel-off approaches to a constant that is related to the apparent adhesion work. In practice, the length of the film will be finite. In this section, the peeling force is initially applied near $X = P$ is considered, which we call near-field peeling.

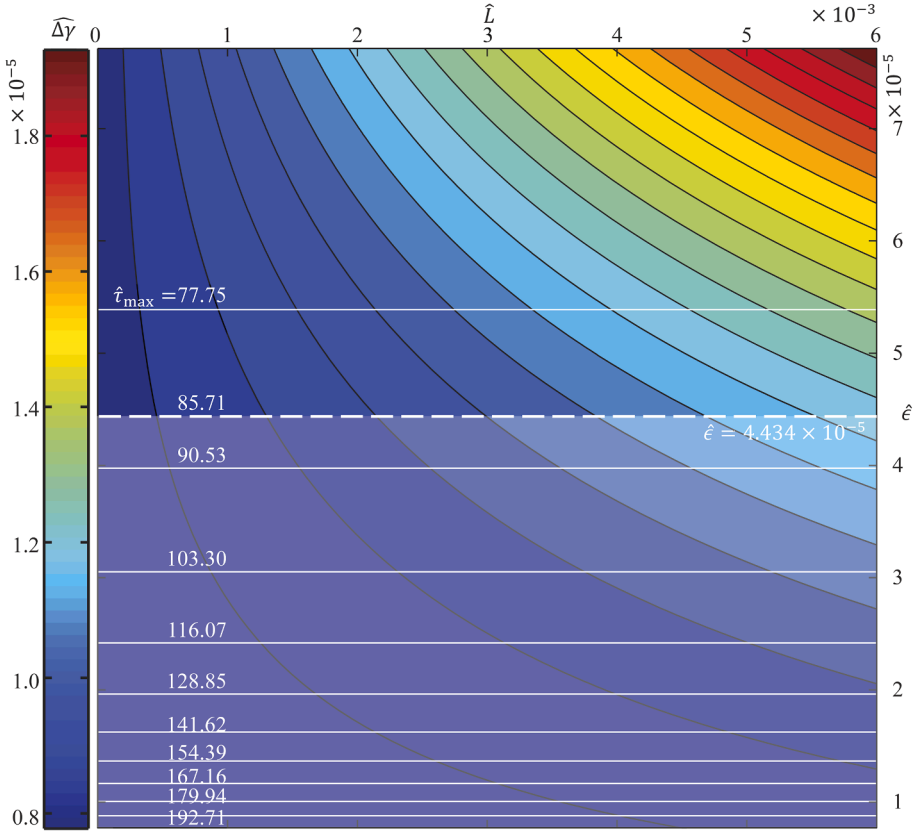

Fig. 16. Map of $\widehat{\Delta\gamma}$ (the rainbow contour nephogram) and $\hat{\tau}_{max}$ (the white contour lines) with respect to $\hat{\epsilon}$ and $\hat{L}$ ($\hat{L} \gg \hat{\epsilon}$).

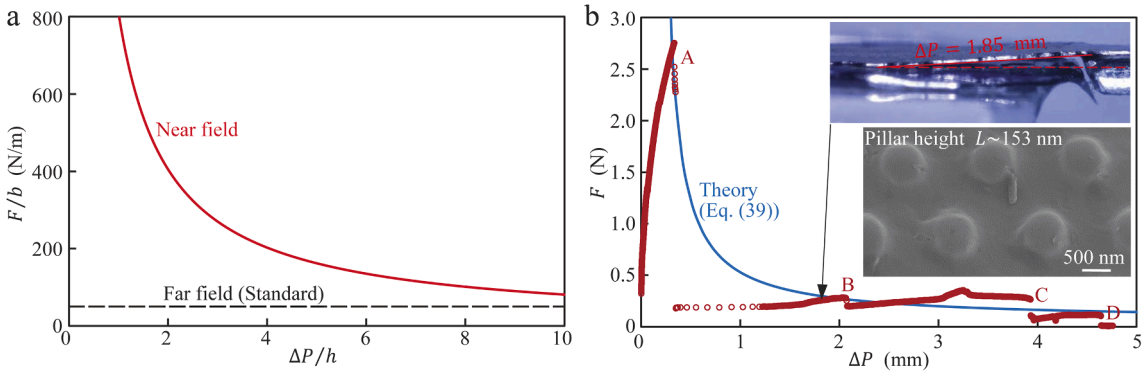

Fig. 17. (a) Comparison of the peeling force under near-field and far-field (i.e., standard) peeling (The peeling angle is $\alpha = \pi/2$). (b) Typical results for the peeling of a structured interface, where the peeling force was recorded by the software of the SEM tester 100 and the cracking distance ΔP was monitored with an optical microscopy. The insets show one frame of the peeling-off process, and the image of Pt nanopillars after mechanical demoulding. The nanopillar height was measured as $L \sim$ 153 nm. The apparent adhesion work $\overline{\Delta\gamma}$ is fitted as 3.7 N/m by Eq. (39) (E=94.8 GPa, ν=0.42 (Wang, 2012); h and b refer to Fig. 1(d)).

Taking the common peeling angle of $\alpha = \pi/2$ for example (Fig. 1(e)). The sectional shear force and moment at $X = P$ are $Q_P = -F$ and $M_P = F\Delta P$, respectively, where ΔP is the distance between the point at $X = P$ and the loading point (Fig. 1(e)). Such a near-field peeling can be associated with the standard peeling model (considering $\alpha_{st} \gg \theta_P$)

$$\begin{cases} M_P = F\Delta P = 2\sqrt{DbF_{st}}\sin\dfrac{\alpha_{st}}{2}, \\ Q_P = -F = -F_{st}\sin\alpha_{st}. \end{cases} \tag{37}$$

where F_{st} and α_{st} are the equivalent peeling force and the peeling angle, respectively. Then we have

$$F_{st} = \frac{F^2\Delta P^2}{4Db} + \frac{Db}{\Delta P^2}, \tag{38a}$$

$$\sin\alpha_{st} = \frac{F}{F_{st}}, \tag{38b}$$

and

$$\tan\frac{\alpha_{st}}{2} = \frac{F\Delta P^2}{2Db}. \tag{38c}$$

Eq. (38a) indicates that $F_{st} \geq F > 0$, and Eqs. (38b) and (38c) guarantee that α_{st} has only a unique solution in the range of $(0, 2\pi)$. As a result, for a given F and ΔP in the near-field peeling, there is a unique corresponding real solution of F_{st} and $\alpha_{st} \in (0, \pi) \subset (0, 2\pi)$. In other words, any near-field peeling problem can be transformed into a specific standard peeling problem. Thus, according to Eq. (24), we have

$$\frac{F}{b} = \frac{h}{\Delta P}\sqrt{\frac{Eh\overline{\Delta\gamma}}{6(1-\nu^2)}} = \frac{3\rho_M Eh^2}{4(7+6\nu)\Delta P}\sqrt{\widehat{\Delta\gamma}}. \tag{39}$$

Eq. (39) tells that the peeling force at the near-field peeling may become extremely large when $\Delta P \to 0$, and it will get worse if the film has a large bending stiffness. Based on Eqs. (2) and (39), a comparison of the peeling force between the far-field and the near-field peeling is shown in Fig. 17(a), where we set $E = 70$ GPa, $h = 1$ μm, $\nu = 1/3$, $\overline{\Delta\gamma} = 50$ N/m, and $\alpha = \pi/2$. As $\Delta P/h$ increases, the required peeling force in the near-filed peeling drastically decreases and finally tends to the far-field peeling force.

Experimentally, the predicted scaling law of $F \propto 1/\Delta P$ (Eq. (39)) could be investigated based on the set-up in Fig. 1(e). Typical results for the peeling of a Pt-BMG strip which was formed into a Ni-BMG mold with surface nanocavities is shown in Fig. 17(b). It is interesting that the peeling process during mechanical demoulding can be regarded as the repetition of the following two processes: gradually debonding to stop at a certain peeled distance of ΔP_{cr} (such as Points A-D in Fig. 17(b)), at which the system is always in force balance though the peeling force increases, until the peeling force increases to a critic value, F_{cr}, the interface starts to debond again. The series of discrete data points (ΔP_{cr}, F_{cr}) reveal the dependence of the steady-state peeling force on the peeling distance, which agrees well with the theoretical prediction (Eq. (38)).

4. Closing remarks

Through theoretical analysis and experiments, the peeling mechanics of film-substrate system with mutually embedded nanostructures in the interface are comprehensively and systematically studied in this work. By integrating the obtained micromechanical behavior in the microstructured interface into the traditional theory of Euler-Bernoulli beam, we derive a concise governing equation for the mechanical demoulding as $\mathrm{d}^4\widehat{\zeta}/\mathrm{d}\widehat{X}^4 - \mathrm{d}/\mathrm{d}\widehat{X} \bullet \mathrm{d}\widehat{\zeta}/(\widehat{\zeta}\mathrm{d}\widehat{X}) + 1 = 0$ ($\widehat{\zeta}$ and $\widehat{X}$ are the dimensionless deflection and the spatial coordinate, respectively), where the factor $1/\widehat{\zeta}$ leads to a mathematical singularity and reveals a strong in-plane shear effect. Considering that the edge of mold cavities is always filleted in real situation (with a dimensionless radius of $\widehat{\epsilon}$), the difficulties in solving the governing equation are greatly reduced, based on which simple expressions for predicting the apparent adhesion work and the maximum interface shear stress are obtained. The expressions establish the quantitative basis for evaluating and guiding the mechanical demoulding process, and predicting the required peeling force. The results presented in this work provide beneficial insights into the physical process and mechanism of interfacial peeling of complex film-substrate systems. Considering that surface/interface structures and thin film-substrates widely exist in nature and man-made systems, these findings could not only deepen the understanding of the peeling mechanics of complex interfaces, but also promote the wide application of nanostructures fabricated by nanomolding.

Declaration of Competing Interest

The authors declare that they have no known competing financial interests or personal relationships that could have appeared to influence the work reported in this paper.

Acknowledgements

This research was supported by the National Natural Science Foundation of China (11902226, 12172260 and 11872284), and the Key Research and Development Program of Hubei Province (2021BAA192).

References

Barthel, E., 2008. Adhesive elastic contacts: JKR and more. J. Phys. D: Appl. Phys. 41, 163001.
Chiu, H.M., Kumar, G., Blawzdziewicz, J., Schroers, J., 2009. Thermoplastic extrusion of bulk metallic glass. Scr. Mater. 61 (1), 28–31.
Chou, S.Y., Krauss, P.R., Renstrom, P.J., 1996. Imprint Lithography with 25-Nanometer Resolution. Science 272 (5258), 85–87.
Chou, S.Y., Krauss, P.R., Zhang, W., Guo, L., Zhuang, L., 1997. Sub-10 nm imprint lithography and applications. J. Vac. Sci. Technol., B 15, 2897–2904.
Creton, C., Ciccotti, M., 2016. Fracture and adhesion of soft materials: a review. Rep. Prog. Phys. 79, 046601.
Dalbe, M.-J., Santucci, S., Cortet, P.-P., Vanel, L., 2014. Strong dynamical effects during stick-slip adhesive peeling. Soft Matter 10 (1), 132–138.
Gent, A.N., Petrich, R.P., 1969. Adhesion of viscoelastic materials to rigid substrates. P Roy Soc. A 310, 433–448.
Ghatak, A., Mahadevan, L., Chung, J.Y., Chaudhury, M.K., Shenoy, V., 2004. Peeling from a biomimetically patterned thin elastic film. P Roy Soc. A 460 (2049), 2725–2735.
Golden, K., Jerzy, B., Jan, S., 2013. Controllable nanoimprinting of metallic glasses: effect of pressure and interfacial properties. Nanotechnology 24, 105301.
Graham, L.W.C., 2006. The production of nanostructures by mechanical forming. J. Phys. D: Appl. Phys. 39, R363–R386.
Guduru, P.R., Bull, C., 2007. Detachment of a rigid solid from an elastic wavy surface: Experiments. J. Mech. Phys. Solids 55 (3), 473–488.
Guo, L.J., 2004. Recent progress in nanoimprint technology and its applications. J. Phys D Appl. Phys. 37, R123-R141.
Israelachvili, J., 1992. Interfacial Forces. J. Vac. Sci. Technol., A 10 (5), 2961–2971.
Kaelble, D.H., 1971. Cavitation in viscoelastic media. Trans. Soc. Rheol. 15 (2), 275–296.
Kaelble, D.H., 1992. Theory and analysis of peel adhesion - adhesive thickness effects. J. Adhesion. 37 (1-3), 205–214.
Kendall, K., 1971. The adhesion and surface energy of elastic solids. J. Phys. D Appl. Phys. 4, 1186–1195.
Kendall, K., 1975. Thin-film peeling-the elastic term. J. Phys. D Appl. Phys. 8 (13), 1449–1452.
Khandeparker, L., Anil, A.C., 2007. Underwater adhesion: The barnacle way. Int. J. Adhes. Adhes. 27 (2), 165–172.
Kinloch, A.J., Williams, J.G., 2002. The mechancis of peel tests. The mechanics of adhesion (D.A. Dillard & A.V. Pocius eds.), pp. 273-301. Boston: Elsevier.
Kong, D., Ji, B., Dai, L., 2008. Nonlinear mechanical modeling of cell adhesion. J. Theor. Biol. 250 (1), 75–84.
Kumar, G., Tang, H.X., Schroers, J., 2009. Nanomoulding with amorphous metals. Nature 457 (7231), 868–872.
Li, N., Chen, W., Liu, L., 2016. Thermoplastic Micro-Forming of Bulk Metallic Glasses: A Review. JOM 68 (4), 1246–1261.
Li, S., Yao, Q., Li, Q., Feng, X.Q., Gao, H., 2018. J. Mech. Phys. Solids 111, 277–289.
Liu, N., Xie, Y., Liu, G., Sohn, S., Raj, A., Han, G., Wu, B., Cha, J.J., Liu, Z., Schroers, J., 2020. General nanomolding of ordered phases. Phys. Rev. Lett. 124, 036102.
Liu, Z., 2017. One-step fabrication of crystalline metal nanostructures by direct nanoimprinting below melting temperatures. Nat. Commun. 8, 14910.
Liu, Z., 2019. Investigation of temperature and feature size effects on deformation of metals by superplastic nanomolding. Phys. Rev. Lett. 122, 016101.
Liu, Z., Han, G., Sohn, S., Liu, N., Schroers, J., 2019. Nanomolding of crystalline metals: the smaller the easier. Phys. Rev. Lett. 122, 036101.
Liu, Z., Liu, N., Schroers, J., 2022. Nanofabrication through molding. Prog. Mater. Sci. 125, 100891.
Liu, Z., Schroers, J., 2015. General nanomoulding with bulk metallic glasses. Nanotechnology 26, 145301.
Menga, N., Afferrante, L., Pugno, N.M., Carbone, G., 2018. The multiple V-shaped double peeling of elastic thin films from elastic soft substrates. J. Mech. Phys. Solids 113, 56–64.
Muller, V.M., 1999. On the theory of pull-off of a viscoelastic sphere from a flat surface. J. Adhes. Sci. Technol. 13 (9), 999–1016.
Obreimoff, J.W., 1930. The splitting strength of mica. P Roy. Soc. A 127, 290–297.
Peng, Z., Chen, S., 2015. Peeling behavior of a thin-film on a corrugated surface. Int. J. Solids Struct. 60–61, 60–65.
Persson, B.N.J., Brener, E.A., 2005. Crack propagation in viscoelastic solids. Phys. Rev. E 71, 036123.
Rivlin, R.S., 1944. The effective work of adhesion. Paint Technol. 9, 215–218.
Shui, L.Q., Jia, L.B., Li, H.B., Guo, J.J., Guo, Z.Y., Liu, Y.L., Liu, Z., Chen, X., 2020. Rapid and continuous regulating adhesion strength by mechanical micro-vibration. Nat. Commun. 11, 1583.
Shull, K.R., 2002. Contact mechanics and the adhesion of soft solids. Mat. Sci. Eng. R 36 (1), 1–45.
Singer, J.P., Gopinadhan, M., Shao, Z., Taylor, A.D., Schroers, J., Osuji, C.O., 2015. Nanoimprinting Sub-100 nnn Features in a Photovoltaic Nanocomposite using Durable Bulk Metallic Glass Molds. ACS Appl. Mater. Inter. 7, 3456–3461.
Tiwari, A., Dorogin, L., Bennett, A.I., Schulze, K.D., Sawyer, W.G., Tahir, M., Heinrich, G., Persson, B.N.J., 2017. The effect of surface roughness and viscoelasticity on rubber adhesion. Soft Matter 13 (19), 3602–3621.
Villey, R., Creton, C., Cortet, P.-P., Dalbe, M.-J., Jet, T., Saintyves, B., Santucci, S., Vanel, L., Yarusso, D.J., Ciccotti, M., 2015. Rate-dependent elastic hysteresis during the peeling of pressure sensitive adhesives. Soft Matter. 11 (17), 3480–3491.
Wang, W.H., 2012. The elastic properties, elastic models and elastic perspectives of metallic glasses. Prog. Mater Sci. 57 (3), 487–656.
Xia, Y., Whitesides, G.M., 1998. Soft lithography. Annu. Rev. Mater. Sci. 28 (1), 153–184.
Xu, L., Shui, L., Zhang, Y., Peng, Q., Xue, L., Liu, Z., 2020. Robust and reproducible fabrication of large area aluminum (Al) micro/nanorods arrays by superplastic nanomolding at room temperature. Appl. Phys. Express 13, 036503.
Yin, J., Zhao, Y.-P., Zhu, R.-Z., 2005. Molecular dynamics simulation of barnacle cement. Mat. Sci. Eng. A-Struct. 409 (1-2), 160–166.
Yu, S.-J., Li, S.-C., Ni, Y., Zhou, H., 2017. Size dependent morphologies of brittle silicon nitride thin films with combined buckling and cracking. Acta Mater. 127, 220–229.